Theory of Flame Front Propagation in Porous Propellant Charges under Confinement

K. K. KUO,* R. VICHNEVETSKY,† AND M. SUMMERFIELD‡
Guggenheim Aerospace Propulsion Laboratories, Princeton University, Princeton, N.J.

Ultra-high burning rates can be achieved by combustion of porous media. A theoretical model is developed to describe the flame propagation in a packed bed of granular propellant. The calculated pressure-time-distance transients, wave propagation speed, and mass fraction of propellant burned during flame propagation, all agree well with experimental data obtained for the same conditions. Results demonstrate that the combustion-generated strong pressure gradient causes the hot product gas to deeply penetrate the unburned region. A continental divide forms automatically in the pressure distribution as the wave progresses into the charge. In the particular case studied, after traversing a distance of 3 cm, the flame front reaches a speed about 5000 times the normal propellant burning rate and continues to accelerate as the internal pressure increases.

Nomenclature

a = pre-exponential factor for burning rate law
A = cross-sectional area of the porous bed
c_d = deterrent concentration
c_p = specific heat at constant pressure
C = speed of sound
D = drag force acting on gases by the pellets per unit wetted area of pellets
E = total stored energy per unit mass
F = function defined in Eq. (35)
g = inhomogeneous terms in the characteristic equation
G = inhomogeneous terms in the governing equation
h_c = the average heat transfer coefficient over pellets
h_f = enthalpy of gas at adiabatic flame temperature
k = thermal conductivity of gases
k_p = thermal conductivity of pellets
$\dot{m}_{\text{ign}}$ = mass flow rate of igniter
n = number density of spherical pellets in the packed bed or exponent for the burning rate law
P = pressure
P_c = pressure at void chamber
Pr = Prandtl number
P_w = wetted perimeter
q_l = heat loss to the tube wall
r = radius
r_b = burning rate of the solid propellant
r_p = radius of pellets
r_t = tube radius
R = gas constant
Re = Reynolds number
t = time
T = temperature
T_c = temperature at void chamber
T_f = adiabatic flame temperature of pellets
T_{ign} = temperature of the igniter gas
T_{ps} = temperature of the pellet surface
T_o = initial temperature of pellets
U = gas velocity
V = 3-vector defined by Eq. (36)
x = distance from igniter face
x_e = length of the cylindrical chamber
x_p = position at the entrance of the porous bed
α_p = thermal diffusivity of pellets
γ = specific heat ratio
θ = weighting parameter for the implicit numerical scheme ($0 \leq \theta \leq 1$)
μ = gas viscosity
ρ = gas density
ρ_p = density of pellets
τ_w = shear stress on the tube wall
ϕ = fractional porosity (percentage of the void volume)
ψ = a function of time defined by Eq. (26)

Subscripts

g = gas phase
i = initial value
n = index for discrete points in the spatial direction $x_n = n\Delta x$
o = original condition or cold end condition
p = based upon pellet diameter or signifying pellets
I = along right-running characteristics
II = along left-running characteristics
III = along particle path-line

Superscripts

j = index for discrete time increments, $t^j = j\Delta t$
p = values obtained in the predictor calculations

Introduction§

PRACTICAL solid propellants normally burn at rates of 1–10 cm/sec at pressures of 100 atm. In many applications, however, propellants with much higher burning rates of 20–50 cm/sec

Presented as Paper 71-210 at the AIAA 9th Aerospace Sciences Meeting, New York, January 25–27, 1971; submitted March 20, 1972; revision received August 18, 1972. This work was performed in part under Contract N00014-67-A-0151-0023 issued by the Power Branch of the Office of Naval Research. The authors wish to give their gratitude especially to W. H. Squire of Frankford Arsenal, U.S. Army, for some valuable discussions and also for providing them with many pertinent experimental results so that a comparison between the theoretical prediction and the actual firing data became possible. T. O. Williams was very helpful in numerical analysis and in programing of the equations for the computer.

Index categories: Combustion in Heterogeneous Media; Combustion Stability, Ignition, and Detonation.

* Post-Doctoral Research Associate, Department of Aerospace and Mechanical Sciences, Princeton University; presently Assistant Professor of Mechanical Engineering, Pennsylvania State University. Member AIAA.

† Professor of Computer Science, Rutgers University, Consultant, Princeton University. Associate Fellow AIAA.

‡ Professor of Aerospace Propulsion. Fellow AIAA.

§ The original manuscript had a rather extensive review of previous published work on flame propagation in porous charges, on the correlation of such critical conditions in terms of dimensionless physical groups, and on the various studies made on the mechanisms of accelerated waves. It was removed in order to save printing space, but copies can be obtained by writing to one of the authors.

at 100 atm and 100–250 cm/sec at 1000 atm are required. Propellant chemists have directed their efforts over the years to searching for energetic and/or catalytic additives to achieve such high rates. However, this paper is concerned with a different approach to this problem, one that is physical rather than chemical in nature.

In order to obtain the desired ultra-high burning rates just prescribed, the convective mode of energy transfer is considered; this is because it is far more effective than the slow conductive mode of energy transfer which governs the burning rate of most conventional propellants. Convective heat transfer can be achieved easily in a porous propellant. It can either be a cast monolithic propellant with pores or a packed bed of granular pellets. The hot gas produced by combustion in such a bed can be driven into the unburned portions by the pressure gradients generated on the end surface of the charge or inside the porous propellant grain. The advantage of using porous propellant is two-fold; one is to attain strong and effective heat feedback from burned products to the cold unburned propellant so that the speed of flame propagation is increased, the other is to have a larger burning area so that high gasification rates can be achieved. Due to these significant potentials for producing the required ultra-high burning rates, the subject of porous propellant combustion and the associated hazard of spontaneous transition from deflagration to detonation have been an area of considerable interest.

Experimental evidence from the burning of confined columns of porous explosives indicates that the over-all transient burning behavior from deflagration to detonation can generally be divided into four stages.[1,2] In the normal burning state, combustion propagates by heat conduction. Because of the penetration of gaseous products into the pores of the explosives, combustion carries over to the convective stage. After the flame has been accelerated for some distance in this convective burning state, combustion then takes place in the low-velocity detonation stage; appearance of the latter stage depends upon experimental conditions. Finally, a shock wave is formed which causes the abrupt transition into a true detonation.

Combustion proceeding by the conductive mechanism of energy transfer has been studied quite thoroughly and is well understood. However, the burning in the subsequent stages is still not yet clear, since different stages of combustion are governed by different mechanisms of energy transfer. In addition, the transitions from one stage to another are due to different physical effects. As a result, it would be extremely difficult to set up a single theoretical model which would describe the over-all transient combustion process. It is believed that without fully understanding the transient processes occurring in the early stages, no fruitful results can be directly obtained in studying transition in the later stages.

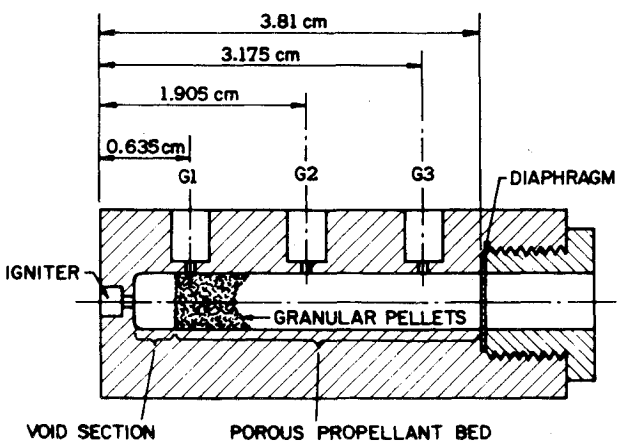

Fig. 1 Configuration considered in the physical model.

The purpose of this research is to give a better understanding of the convective burning and self-accelerating nature of the flame front in a packed bed of granular propellant. Comparisons between the theoretical results and Squire's[3] previously reported firing test data with cylinders of packed ball powder are made. Extremely good agreements are obtained, not only in the various recorded pressure transients, but also in the observed wave travel time and the measured amount of propellant consumed during flame propagation.

Although the analysis does not cover the complete range of DDT (deflagration-to-detonation transition),[4-19] the theoretical results for the final stages of the convective burning process do provide much useful information for interpreting the early part of the transition-to-detonation process.

Even the convective mode of burning which has been studied quite extensively in various experiments is still not yet completely understood. No sound analytical approach has been developed. This is probably due to the extremely complicated phenomena involved in the transient burning processes. Physically, the rate of gasification of a porous propellant is strongly coupled with both the flow conditions in the gas phase and the heat transfer conditions in the solid phase. The wave front controlled by the combustion of explosives, in turn, affects the penetration of the hot product gas and hence the heat transfer to the solid. Mathematically, the basic partial differential equations describing unsteady flow of gases through porous media are nonlinear and inhomogeneous, and no simple closed-form solutions for specified boundary and initial conditions can be derived. In addition, the empirical relations that would be required to describe the heat transfer and the flow resistance in such a theory are not generally available for the cases considered.

With the advent of the modern high-speed digital computer and some recent developments in numerical schemes, it appears promising to set up a theoretical model which can be solved by numerical methods.

Analysis

Physical Model Description

The model analyzed here is constructed to represent the following test conditions. An adiabatic cylindrical chamber (of diameter 0.951 cm and length 3.81 cm) packed with deterred spherical pellets is considered (Fig. 1). At the left end of the chamber, there is an igniter which provides a flow of hot gas into the (plenum) void section, located at the entrance to the porous medium. The void section serves as a reservoir for the high temperature gas that flows into the packed bed of spherical pellets. At the right end of the chamber, there is a diaphragm (with thickness 0.762 mm) which keeps the chamber closed until a pressure of about 0.75 kbar is reached.

As the igniter gas is turned on, a fraction of the hot igniter gas flows from the plenum into the porous bed, heating the granular pellets and eventually bringing some of them to the ignition condition. A combustion wave then starts at the upstream end of the propellant bed. As the ignition front moves downstream, more hot reacted gas is generated by the combustion of the pellets. The pressure in the combustion zone increases drastically due to the gasification processes on the burning pellets surfaces. The rise in pressure will, in turn, cause the regression rate to increase. Furthermore, the pressure rise in the combustion zone elevates both the pressure gradient at the ignition front and the level of gas density there. Hence more hot gas is driven into the unburned region. This increases the rate of heat transfer to the pellets ahead of the ignition front. The still unburned pellets are heated up more and more rapidly. The ignition front, therefore, moves toward the downstream direction in an accelerated manner.

As the ignition front propagates downstream, a severe burning zone in the upstream is created. This is due to the accumulation of product gas which is generated in the middle of the instantaneous combustion zone, since not all the product gas can pass through the ignition front and flow into the unburned region.

In addition, the pellets on the left end of the porous bed have been burning for a longer time than the pellets downstream. The total burning area is smaller at the upstream portion and hence can contribute less product gas. This effect is further magnified by the burning rate law. Therefore, a reverse pressure gradient exists at the left end of the burning zone and a forward pressure gradient exists at the right end of the burning zone. A continental divide in the $p(x)$ curve is hence generated. The product gas, on the left-hand side of the continental divide, flows from the combustion zone in the opposite direction, compressing the gas in the plenum. Following the propagation of the ignition front, the continental divide moves gradually toward the diaphragm. Because severe burning occurs in the peak pressure region, the continental divide is usually quite gentle, especially when the small loading density cases are considered. The appearance of continental divide in the $p(x)$ curve is an expected feature of porous propellant burning.

Basic Assumptions

There are three basic assumptions pertinent to the present analysis: a) Propellant grains are considered to be fixed in space, as in a firmly compacted and cemented propellant bed. This assumption drastically reduces the difficulties in the analysis. Without it, the conservation equations for a mobile condensed phase must be solved together with the gas phase equations. The validity of this assumption is given in the section labeled Discussion of Results. b) The life time of a pellet is considered to be much longer than the time for an ignition front to propagate through many columns of pellets. This assumption permits the consideration of the gas properties inside the reaction zone as continuous functions of the space variable x. Experimental evidence in some practical cases confirms that the flame zone is very thick. c) The flow in the porous medium is considered to be one dimensional. According to Gipson and Mecek[13] there is only a little irregularity in the time-distance plot of spirally placed ionization probes. This verifies that the flame front is approximately planar and perpendicular to the charge axis throughout the buildup to detonation in their experiments. The one-dimensional approach has been commonly used in the study of deflagration to detonation transition,[10,13-16] although, there are cases where the observed flame fronts are not really planar and steady. Uneven fronts are often observed in the convective burning regime.[8,17-19] This is due to uneven penetrations of the flame into the interstitial voids in the porous charge. Analysis of such a complicated problem is unjustified at the present time.

Description of the Mathematical Model

The mass conservation equation is

$$\partial(\rho\phi)/\partial t+\partial(\rho\phi U)/\partial x=[3(1-\phi)/r_p]\rho_p r_b \tag{1}$$

The momentum equation is

$$\frac{\partial(\rho\phi U)}{\partial t}+\frac{\partial(\rho\phi U^2)}{\partial x}=\frac{\partial}{\partial x}\left(\frac{4}{3}\mu\phi\frac{\partial U}{\partial x}\right)-\phi\frac{\partial P}{\partial x}-\frac{P_w\tau_w}{A}-\frac{3(1-\phi)}{r_p}D \tag{2}$$

The energy equation written in terms of the total stored energy per unit mass, E is

$$\frac{\partial(\rho\phi E)}{\partial t}+\frac{\partial(\rho\phi UE)}{\partial x}=-\frac{\partial(\phi UP)}{\partial x}+\frac{\partial}{\partial x}\left(k\phi\frac{\partial T}{\partial x}\right)+\frac{\partial}{\partial x}\left(\frac{4}{3}\mu\phi U\frac{\partial U}{\partial x}\right)-\frac{2q_l}{r_t}+\frac{3(1-\phi)}{r_p}[\rho_p r_b h_f-h_c(T-T_{ps})] \tag{3}$$

The above conservation equations constitute a set of inhomogeneous, nonlinear, partial differential equations. In order to solve the problem economically, further simplifications are considered.

After an order-of-magnitude analysis, the influence of following terms is neglected a) heat loss to the tube wall, b) friction force exerted on the gas by the tube wall, c) work done due to viscous stress generated from the velocity gradient in the axial direction, d) heat dissipative term, e) molecular heat conduction from gas to gas in the axial direction, f) imperfections in the gas equation of state, g) temperature dependence of constant pressure specific heat, h) dynamic burning effect on the burning rate, i) temperature sensitivity effect on burning rate, and j) erosive burning effect on burning rate.

After rearranging the mass and energy equations, and inserting the perfect gas law the following set of governing equations is obtained

$$\frac{\partial U}{\partial t}+U\frac{\partial U}{\partial x}+\frac{1}{\rho}\frac{\partial P}{\partial x}=-\frac{3(1-\phi)}{r_p\phi\rho}\{r_b U\rho_p+D\} \tag{4}$$

$$\frac{\partial T}{\partial t}+U\frac{\partial T}{\partial x}+(\gamma-1)T\frac{\partial U}{\partial x}=-\frac{(\gamma-1)TU}{\phi}\frac{\partial\phi}{\partial x}-\frac{3(1-\phi)T}{r_p\phi P}(\gamma-1)h_c(T-T_{ps})+\frac{3(1-\phi)T}{r_p\phi P}\left\{r_b\rho_p\left(\gamma RT_f-RT+\frac{\gamma-1}{2}U^2\right)+(\gamma-1)DU\right\} \tag{5}$$

$$\frac{\partial P}{\partial t}+U\frac{\partial P}{\partial x}+\gamma P\frac{\partial U}{\partial x}=-\frac{\gamma PU}{\phi}\frac{\partial\phi}{\partial x}-\frac{3(1-\phi)}{r_p\phi}(\gamma-1)h_c(T-T_{ps})+\frac{3(1-\phi)}{r_p\phi}\left\{r_b\left(\gamma\rho_p RT_f-P+\frac{\gamma-1}{2}\rho_p U^2+(\gamma-1)DU\right)\right\} \tag{6}$$

The unknowns of these three governing equations are the gas velocity U, temperature T, and pressure P. The fractional porosity ϕ is also an unknown, but since it varies slowly in comparison with U, T, and P, it is calculated separately in terms of instantaneous pellet radius according to the following equation

$$\phi=1-n(\tfrac{4}{3}\pi r_p^3) \tag{7}$$

The instantaneous pellet radius at position x and time t is determined from

$$r_p(t,x)=r_p(0,x)-\int_0^t r_b(\tau,x)\,d\tau \tag{8}$$

Three initial conditions are required for solution to the coupled equations (4), (5) and (6). For an initially uniform quiescent state in the bed, the conditions are

$$U(0,x)=0,\qquad T(0,x)=T_o,\qquad P(0,x)=P_o \tag{9}$$

where T_o and P_o are the initial gas temperature and pressure in the porous bed.

The number of boundary conditions required to specify the physical problem depends upon the flow conditions at both ends of the porous bed.[22,23] Since the current analysis covers only the convective burning processes preceding the burst of the diaphragm, the boundary condition at the diaphragm end of the porous bed is

$$U(t,x_e)=0 \tag{10}$$

When the gas is flowing from the void section into the porous bed, two other boundary conditions should be specified at the entrance x_p to the porous bed. The gas temperature and pressure at x_p are

$$T(t,x_p)=T_c(t)-[U(t,x_p)^2/2C_p] \tag{11}$$

$$P(t,x_p)=P_c(t)[T(t,x_p)/T_c(t)]^{\gamma/(\gamma-1)} \tag{12}$$

The velocity $U(t,x_p)$ is one of the extraneous boundary conditions which is determined by the method of characteristics. The chamber pressure $P_c(t)$ and temperature $T_c(t)$ are determined from the conservation equations for the void section. These conservation equations and their initial conditions are given in the next section.

After the combustion process has started in the porous bed, the igniter mass flow is cut off; the gas pressure at the forward end of the porous bed then rises higher than the chamber pressure, so that a fraction of the hot product gas flows backward into the void section. After the gas velocity $U(t,x_p)$ changes sign from positive to negative values, the boundary condition at x_p is different from that discussed previously. The stagnation temperature at x_p is no longer equal to the gas temperature in the

void section. There is only one boundary condition which is required and available to specify the flow condition at the igniter end of the porous bed. This boundary condition is

$$P(t,x_p) = P_c(t)[1+\{U(t,x_p)^2/2C_pT(t,x_p)\}]^{-\gamma/\gamma-1} \quad (13)$$

From the continuity and energy equation for the void section, the rate of change of stagnation pressure and temperature are derived as

$$\frac{dP_c(t)}{dt} = \frac{\gamma R T_{ign}}{Ax_p}\dot{m}_{ign}(t) - \frac{\gamma R\rho(t,x_p)U(t,x_p)\phi(t,x_p)}{x_p} \times \left[T(t,x_p) + \frac{U(t,x_p)^2}{2C_p}\right] \quad (14)$$

$$\frac{dT_c(t)}{dt} = \frac{RT_c(t)}{Ax_pP_c(t)}\dot{m}_{ign}(t)[\gamma T_{ign} - T_c(t)] - \frac{RT_c(t)\rho(t,x_p)U(t,x_p)\phi(t,x_p)}{x_pP_c(t)}\left[\gamma T(t,x_p) + \gamma\frac{U(t,x_p)^2}{2C_p} - T_c(t)\right] \quad (15)$$

The two initial conditions for this pair of equations are simply

$$P_c(0) = (P_c)_o \quad (16)$$

$$T_c(0) = (T_c)_o \quad (17)$$

It is important to note that the terms on the right-hand side of both Eq. (14) and Eq. (15) do depend upon flow properties and conditions at x_p. Unless the gas velocity, temperature, and pressure are already determined by some other relations, the above pair of ordinary differential equations are always coupled with additional equations which must be solved simultaneously with Eqs. (14) and (15). In searching for these additional relationships, the nature of the governing partial differential equations are studied.

It is found in the study that the eigenvalues of the system are three distinct real numbers under any conditions; the governing equations are hence totally hyperbolic in form. The characteristic directions are described by

$$(dx/dt)_{\rm I} = U+C, \quad (dx/dt)_{\rm II} = U-C, \quad (dx/dt)_{\rm III} = U \quad (18)$$

The characteristic equations along the right- and left-running Mach lines are

$$(dU)_{\rm I,II} = \mp\frac{C}{\gamma P}(dP)_{\rm I,II} - D\frac{3(1-\phi)}{r_p\phi}\frac{C}{\gamma P}[C\mp(\gamma-1)U](dt)_{\rm I,II}\mp \frac{CU}{\phi}\frac{\partial\phi}{\partial x}(dt)_{\rm I,II}\mp h_c\left[\frac{3(1-\phi)(\gamma-1)C(T-T_{ps})}{r_p\phi\gamma P}\right](dt)_{\rm I,II}\pm r_b\frac{3(1-\phi)}{r_p\phi}\left[\frac{C}{\gamma P}(\gamma\rho_pRT_f-P)\mp\frac{U\rho_p}{\rho}+\frac{(\gamma-1)\rho_pCU^2}{2\gamma P}\right](dt)_{\rm I,II} \quad (19), (20)$$

The equation along the particle path-line is

$$(dP)_{\rm III} = \frac{\gamma}{\gamma-1}\frac{P}{T}(dT)_{\rm III} - D\left[\frac{3(1-\phi)U}{r_p\phi}\right](dt)_{\rm III} - r_b\frac{3(1-\phi)}{r_p\phi}\left[\rho_pC_p(T_f-T)+P+\frac{\rho_pU^2}{2}\right](dt)_{\rm III} + h_c\left[\frac{3(1-\phi)}{r_p\phi}(T-T_{ps})\right](dt)_{\rm III} \quad (21)$$

The characteristic equations (19–21) are the additional relationships required to relate the flow properties on the boundary of the domain of interest.

The heat equation for unburned spherical pellets at a fixed location is

$$\partial T/\partial t = (\alpha_p/r)\,\partial^2(rT)/\partial r^2 \quad (22)$$

the initial condition for the heat equation is

$$T(0,r) = T_o \quad (23)$$

Because the thermal wave penetration depth into the propellant for the over-all interval of the pressure transient is only a small fraction of the unburned pellet radius, the temperature at the center of every pellet can be considered constant, i.e.,

$$T(t,0) = T_o \quad (24)$$

The other boundary condition prescribed at the outer surface of the pellet is coupled to the gas phase conditions

$$(\partial T/\partial r)(t,r_p) = [h_c(t)/k_p][T_g(t) - T(t,r_p)] \quad (25)$$

The problem described by Eqs. (22–25) is solved here by an approximate integral method, to obtain the surface temperature T_{ps} required in Eqs. (5, 6, and 19–21). The temperature within a pellet is approximated by

$$T(t,r) = T_o e^{\psi(t)r/r_p} - T_o\psi(t)r/r_p \quad (26)$$

where $\psi(t)$ is an unspecified function of time to be determined through numerical integration. This proposed temperature distribution for various times automatically satisfies the boundary condition at the center of the pellet and simultaneously satisfies the symmetric condition that the temperature gradient at the center be zero. The pellet surface temperature is obtained by setting $r = r_p$ in Eq. (26), that is

$$T_{ps}(t) = T(t,r_p) = T_o[e^{\psi(t)} - \psi(t)] \quad (27)$$

After substituting Eq. (26) into Eq. (22) and performing integration with respect to r from $r = 0$ to $r = r_p$, a first-order ordinary differential equation for $\psi(t)$ is obtained, that is

$$\frac{d\psi(t)}{dt} = \frac{\alpha_p}{r_p^2}\frac{e^{\psi(t)} - \psi(t) - 1 + \frac{r_ph_c(t)}{k_p}\left[\frac{T_g(t)}{T_o} - e^{\psi(t)} + \psi(t)\right]}{e^{\psi(t)}\left[\frac{1}{\psi(t)} - \frac{2}{\psi^2(t)} + \frac{2}{\psi^3(t)}\right] - \frac{2}{\psi^3(t)} - \frac{1}{3}} \quad (28)$$

The initial condition deduced from Eq. (23) is

$$\psi(0) = 0 \quad (29)$$

However, with this initial condition, the solution $\psi(t)$ will be identically zero for all t. To avoid this, the isolated singularity at $t = 0$ is suppressed by setting

$$\psi(0) = \varepsilon \quad (30)$$

where ε is any small number. It is found that in using the assumed temperature profile as a function of time and pellet radius given by Eq. (26), the solution is not sensitive to the value of ε. It is therefore proper to replace the initial condition in Eq. (29) by Eq. (30).

As the pellets are considered to be heated uniformly from all directions, the regression in radius due to the burning of the double base propellant is also taken as uniform. A simple propellant burning rate law

$$r_b = aP^n \quad (31)$$

is used for burning pellets. The burning rate coefficient, a, and exponent, n, are both functions of deterrent concentration at the burning surface. For a given deterrent distribution in a spherical pellet, the deterrent concentration at the instantaneous burning surface is determined uniquely by the instantaneous outer radius of the pellet in question. Hence a and n are implicit functions of pellet radius.

The expression for the drag per unit wetted area of pellets (D) is deduced from the Ergun's equations[20] for the pressure drop correlation in a nonfluidized packed bed of spheres. It is

$$D = (\rho U|U|/6\phi)\{150(1-\phi)/Re_p + 1.75\} \quad (32)$$

Re_p designates the Reynolds number based upon the diameter of pellets. Equation (32) is valid for the Reynolds number range between 1 and 3000 and porosity range between 0.4 and 0.65. The first part in the bracket of Eq. (32) is contributed by the viscous stress and the constant 1.75 is the contribution due to profile drag. The heat-transfer coefficient (h_c) is deduced from Denton's heat transfer correlation[21]

$$Nu_p = 0.8Re_p^{0.7}Pr^{1/3} \quad (33)$$

for flow passing through a packed bed of spheres with Reynolds number in a range between 500 and 50,000 and for porosity around 0.37; h_c is expressed in the following form

$$h_c = 0.65(k/r_p)[\rho|U|\phi r_p/\mu]^{0.7}Pr^{1/3} \quad (34)$$

An ignition criterion which can be easily applied to the propagation of an ignition front over a porous propellant is the attainment of two critical temperatures at the spherical pellet

surfaces. The lower critical value corresponds to the ablation temperature, while the higher one represents the ignition temperature of the solid. This is an extremely simplified view of the complex events that lead to ignition, yet it is still justified, since the time required to heat up a pellet to its ablation temperature is much longer than the time required to reach the full ignition condition (from initial ablation).

Numerical Solution

The equations integrated as a simultaneous system are the three governing equations (4–6), the two equations of the void section (14) and (15), and the pellet surface temperature equation (28). In simple form, the governing equations may be rewritten as

$$\partial V/\partial t = F(V,t)\,\partial V/\partial x + G(V,t) \tag{35}$$

where V is the 3-vector

$$V = \begin{pmatrix} U(t,x) \\ T(t,x) \\ P(t,x) \end{pmatrix} \tag{36}$$

F is a 3×3 matrix of functions, and G is the 3-vector formed by the inhomogeneous terms. To solve the governing partial differential equations numerically, central differences in space and a generalized implicit differences scheme in time are utilized. Let $V_n^j \simeq V(j\Delta t, n\Delta x)$. Then the principle of the differences algorithm may be expressed by

$$\frac{V_n^{j+1}-V_n^j}{\Delta t} = F\cdot\left\{\theta\,\frac{V_{n+1}^{j+1}-V_{n-1}^{j+1}}{2\Delta x} + (1-\theta)\frac{V_{n+1}^{j}-V_{n-1}^{j}}{2\Delta x}\right\} + G \tag{37}$$

where the factor of θ in the right-hand side is implicit, and the factor of $(1-\theta)$ is explicit, and where the nonlinear functions F and G are evaluated at some intermediate point in $[j\Delta t;\ (j+1)\Delta t]$ as described in Eqs. (38) and (39).

Two features of interest of the numerical program are a) the use of a quasilinearization technique to deal with the nonlinearities in the implicit terms of Eq. (37), and b) the treatment of the boundary conditions by a method of characteristics.

Quasi-Linearization and predictor-corrector scheme

A reason for the implicit formulation (37) is in the greatly improved numerical stability properties of this approach. But the implicit equations must be linear in V^{j+1} to allow for the use of regular matrix inversion algorithms. To permit this, the inhomogeneous term G is replaced by linearized forms in a predictor-corrector sequence described by

Predictor

$$\frac{(V_n^{j+1})^p - V_n^j}{\Delta t} = F_n{}^j\left[\theta\,\frac{(V_{n+1}^{j+1})^p-(V_{n-1}^{j+1})^p}{2\Delta x} + (1-\theta)\,\frac{V_{n+1}^j-V_{n-1}^j}{2\Delta x}\right] + G_n{}^j + \theta\left(\frac{\partial G}{\partial V}\right)_n^j (V_n^{j+1}-V_n^j) \tag{38}$$

Corrector

$$\frac{V_n^{j+1}-V_n^j}{\Delta t} = F_n{}^{j+\theta}\left[\theta\,\frac{V_{n+1}^{j+1}-V_{n-1}^{j+1}}{2\Delta x} + (1-\theta)\,\frac{V_{n+1}^j-V_{n-1}^j}{2\Delta x}\right] + G_n{}^j + \theta\left(\frac{\partial G}{\partial V}\right)_n^{j+\theta/2} (V_n^{j+1}-V_n^j) \tag{39}$$

where the $(\ )^{j+\theta}$ quantities are functions of the argument $[\theta(V_n^{j+1})^p+(1-\theta)V_n^j]$ and the $(\ )^{j+\theta/2}$ quantities are functions of the argument $[V_n^j+\theta\{(V_n^{j+1})^p V_n^j\}/2]$.

In each instance, the matrix inversion algorithms utilized to obtain the solution to the linear implicit equations (38) and (39) was the block-tridiagonal factorization method.[24] Because the equations are strongly dominated by the nonlinear inhomogeneous terms, it has been found that the use of predictor-corrector method, combined with the quasilinearization procedure for the treatment of those inhomogeneous terms greatly enhances the stability and accuracy properties of the algorithm.

Extraneous boundary conditions and their treatment

The technique of central differences in space utilized for the hyperbolic system (35) has the property to require that 6 boundary conditions be given, whereas the original equations have their solution defined by 3 boundary conditions only. In fact, it may be shown, that the difference equations (37) are consistent with a hyperbolic system which is not of the third order as the original system (35) is, but of the sixth order (Ref. 25).

The additional boundary conditions required by the difference equations are called extraneous boundary conditions. They are generated in the program by invoking analytical properties of the solution of the governing equations, namely by solving the latter by the method of characteristics at the boundaries. (It should be noted that one-sided differences in space do not generate extraneous boundary conditions. But they become numerically unstable when the direction of flow is reversed, which prevents their use in the present case.) In the subsonic, positive input flow, the two boundary conditions $T(t,x_p)$ and $p(t,x_p)$ are related to the solution of the void section differential equations. There is one left-running characteristic (the Mach-line corresponding to the characteristic value $(U-C)$) along which the compatibility condition is used to generate the extraneous boundary condition $U(t,x_p)$. This compatibility condition is

$$(dU/dt)_{II} = (C/\gamma P)(dP/dt)_{II} + g(P,T,\phi,U) \tag{40}$$

where $g(P,T,\phi,U)$ is the contribution of the inhomogeneous terms, and the total derivatives $(d/dt)_{II}$ are taken along the left-running Mach line. The equation (40) is integrated by a classical Runge-Kutta 4 integration algorithm, in one or two time increments.

When the input flow sign changes, the particle path-line becomes a second left-running characteristic line at x_p. The second extraneous boundary condition is then generated by integration of the compatibility condition along this line in a manner similar to the preceding.

Discussion of Results

Figure 1 represents the test apparatus used by Squire.[3] $G1$, $G2$, and $G3$ are the three pressure gages for recording the pressure traces at the prescribed locations along the porous bed. The recorded data from a typical firing[26] are shown in Fig. 2. These pressure traces indicate that the gage $G1$ senses the compression wave much sooner than the gages at downstream positions. The $G1$ reading after the igniter cutoff (around 0.16 msec) decreases and then after about 0.2 msec increases at a slower rate. This rate of increase of pressure then becomes higher and higher and the pressure reaches a peak value at 0.65 msec. The $G2$ curve after a time lag of 0.25 msec climbs at a faster rate than $G1$ and eventually overtakes it. The $G3$ gage

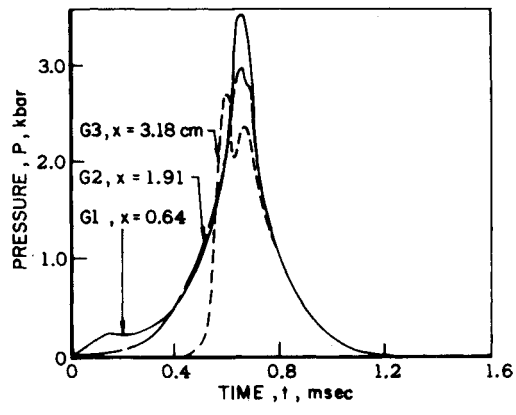

Fig. 2 A typical set of pressure-time traces recorded in Squire's experiments.

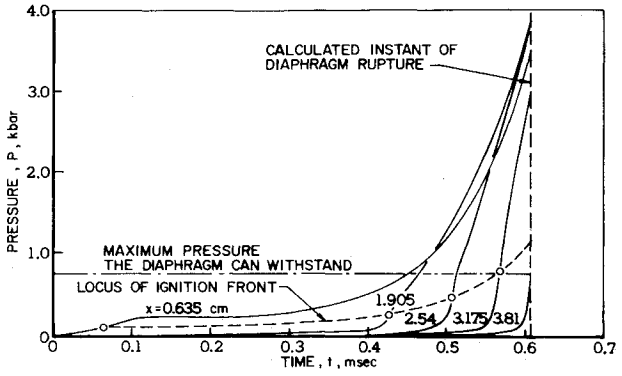

Fig. 3 Predicted readings of pressure time at several locations.

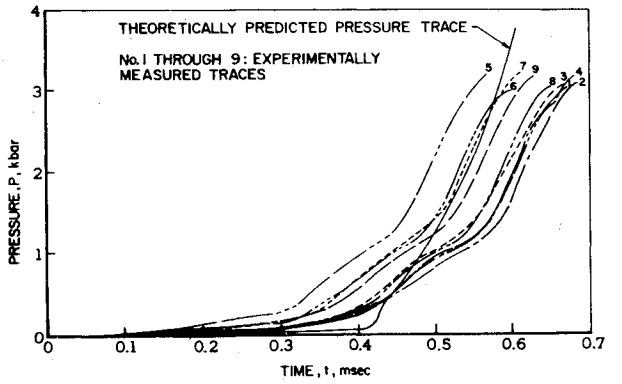

Fig. 5 Comparison between the theoretically predicted pressure-time curve and the experimentally measured traces by gage no. 2 in nine separate firings.

senses the pressure rise the latest and then reaches an extremely sharp rise in pressure. Finally *G*3 overtakes both *G*1 and *G*2.

Due to the inertia of the pellets and also the resistance between the granular bed and the chamber wall, the mobility of pellets is relatively small even under a significant reverse pressure gradient. This results in a further increase in pressure gradient. At 0.6 msec after the onset of igniter flow, the irregularity in the *G*3 curve begins. The decrease in pressure at *G*3 is probably due to the motion of some pellets toward the igniter end of the chamber. The free volume in the upstream portion then becomes smaller and results in a pressure rise in both *G*2 and *G*1. The second peak in the *G*3 curve is generated by the forward pressure gradient, which causes more hot product gas and also some pellets to move toward the diaphragm. At the moment this second peak pressure in *G*3 is reached, the pressure at the diaphragm has just reached the maximum level the diaphragm can withstand, the diaphragm then breaks. From then on, granular propellants together with hot combustion product gases rush out of the chamber. The pressure in the chamber decays and the gradients along the chamber diminish with time. The phenomena after the burst of the diaphragm are not treated in this analysis.

Although it is believed that the pellets do move during the last 0.06 msec interval before the burst of the diaphragm, the motion of pellets is restricted in the very limited space.

In the numerical calculations, the igniter mass flow rate begins with a value of 22.7 g/sec and increases linearly to a constant value of 145.3 g/sec in 0.04 msec. The igniter flow begins to decrease linearly at 0.1 msec and it is completely cutoff at 0.18 msec.

The predicted readings of pressure vs time at several locations are shown in Fig. 3. The calculated pressure trace at the igniter end also shows a pressure hump due to the igniter cutoff. Just as in the experimental data, the pressurization process at the downstream portion produces a faster rate of increase eventually overtaking the upstream pressure trace.

The predicted pressure traces at the corresponding locations of *G*1, *G*2, and *G*3 are individually superimposed on top of experimental data for several separate firings, made with exactly the same test conditions on Figs. 4–6. In Fig. 4, the calculated pressure trace at *G*1 lies just in between these separate firing data. In Fig. 5, a major portion of the predicted pressure trace at *G*2 again lies in between these firing data, but in the early part of the transient solution, the calculated value of pressure is lower than that measured. This is probably due to the fact that the empirical correlation used for the drag term in the packed bed of inert spheres may result in higher resistance than the real test condition. The comparison between experimental and theoretical results in Fig. 6 reveals the same trend. That is, the calculated pressure at *G*3 begins to rise at a later time than the experimentally measured results. Although the comparison at *G*3 is less satisfactory than those at *G*1 and *G*2, the slope of the pressure vs time curve at *G*3 is very close to what was measured. Also, the time lag for the predicted sharp pressure rise at *G*3 is only 11% off from the measured time lag.

Another comparison between the calculated results and the true firing data is made on the rupture time of the diaphragm at the right end of the porous bed. The analytical calculation ceases as soon as the calculated pressure at the diaphragm reaches a critical value of 0.75 kbar. According to the calculated results, the diaphragm breaks at 0.609 msec which is in very close agreement with the average value of 0.64 msec from the actual measured rupture times in these separate firings. Note that the measured rupture time ranges from 0.565 msec to 0.682 msec so

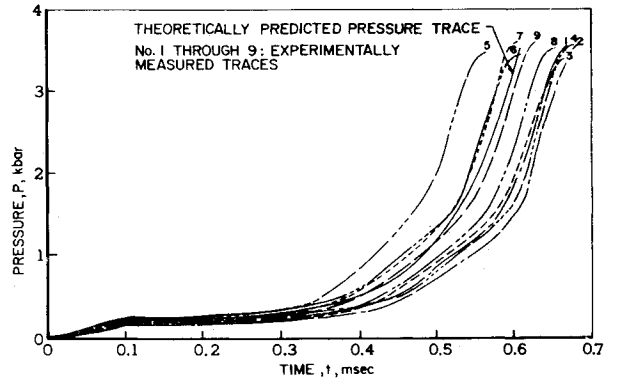

Fig. 4 Comparison between the theoretically predicted pressure-time curve and the experimentally measured traces by gage no. 1 in nine separate firings.

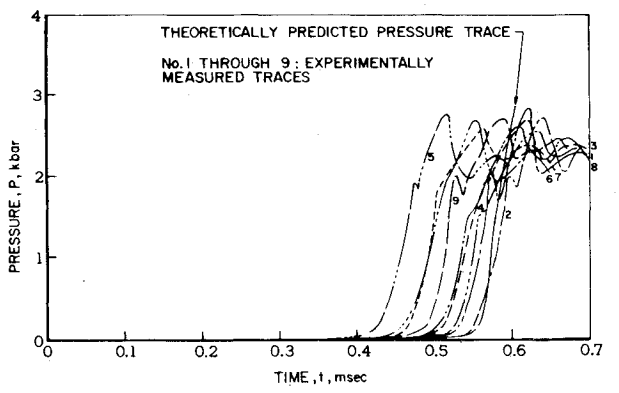

Fig. 6 Comparison between the theoretically predicted pressure-time curve and the experimentally measured traces by gage no. 3 in nine separate firings.

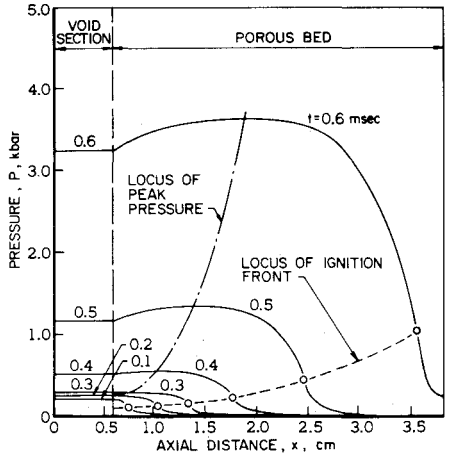

Fig. 7 Calculated pressure distribution at various times.

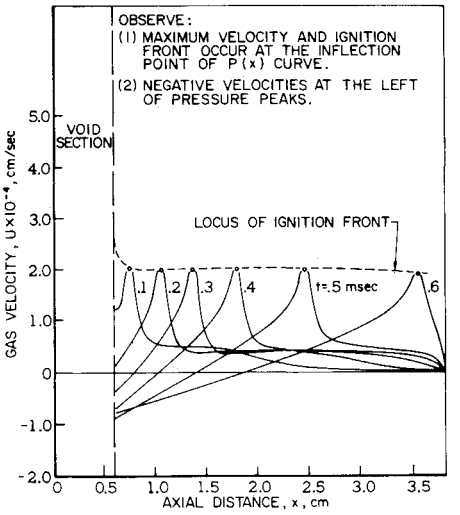

Fig. 9 Calculated gas velocity distribution at various times.

that the theoretical prediction is actually within experimental accuracy.

In addition, the calculation shows that only 19.8% of the propellant in the chamber is consumed before the rupture of the diaphragm. This result is also in good agreement with the measured value of around 16%.

The calculated pressure distributions at various times are shown in Fig. 7. The variations in pressure distributions delineate an acceleration of pressurization everywhere inside the chamber. The effect of increase in the rate of pressurization is most pronounced near the right end of the chamber. The locus of ignition front passes through the inflected points on $P(x)$ curves. The highest pressure gradient occurs at the ignition front, because the pressure gradients are effectively reduced due to heat release processes in the burning zone behind the ignition front, and also the pressure decays along the axial direction in penetrating the porous medium. Following the advancement of the ignition front, the continental divide, created from gaseous accumulation in the middle of the burning zone, moves also toward the right end of the chamber.

Along the locus of ignition front, the pressure gradient increases with time. This is mainly caused by the pressurization processes behind the ignition front. The effect of steepening in the pressure profile at the combustion wave front facilitates the penetration of the hot product gas into the unburned region. At the left side of the continental divide, the product gas driven by the reverse pressure gradient flows into the void section. Since the gas inside the void section is assumed to be homogeneous, the calculated pressures for various times in the void section is uniform.

The calculated temperature distribution at the times corresponding to those in Fig. 7 are plotted in Fig. 8. The temperature in the combustion zone is more or less constant, except in the void section and its neighboring region. The higher temperatures in these portions are due to the chamber filling and compression effect produced by the reverse pressure gradient on the left-hand side of the continental divide. Because of the strong cooling effect in front of the ignition point, the gas temperature drops sharply to the ambient temperature. The temperature rise at the diaphragm is mainly due to the compression effect. This compression effect ahead of the flame is created by the acceleration of convective burning, which becomes more pronounced as the ignition front approaches the diaphragm.

In Fig. 9, the velocity distributions at various times are plotted. The peaks in these velocity distributions are generated by the maximum pressure gradients at the inflection points on the pressure distributions. Therefore, the locus of ignition front on the velocity distributions connects the peaks at various times.

Figure 10 shows the calculated position and speed of flame front versus time. After the igniter cutoff effect, the ignition front accelerates very rapidly in the axial direction. Close to the diaphragm, the acceleration is on the order of 1.2×10^6 m/sec^2.

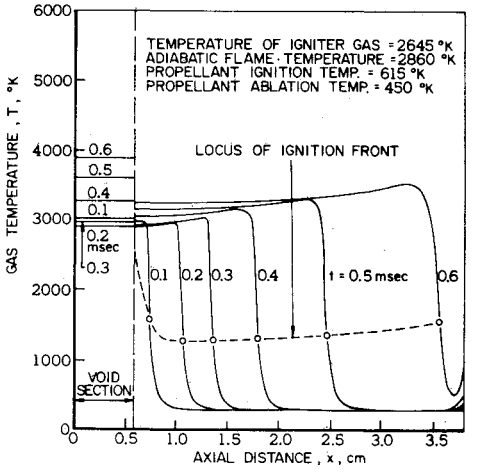

Fig. 8 Calculated gas temperature distribution at various times.

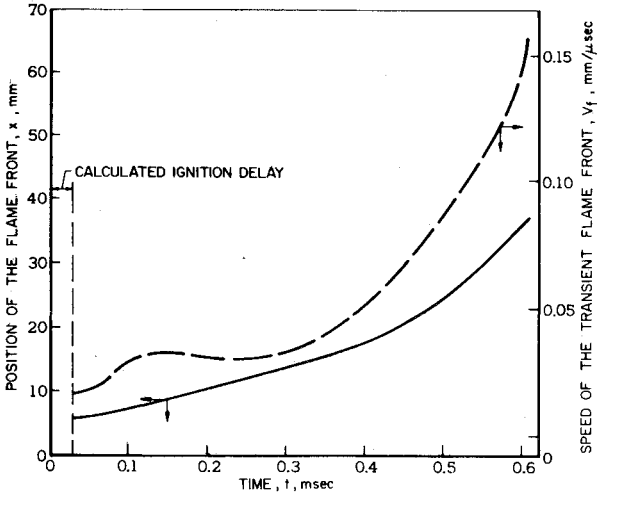

Fig. 10 Calculated position and speed of the flame front as a function of time.

Conclusions

1) A successful theoretical model has been developed to describe the transient flame spreading and convective burning processes in a packed bed of granular pellets. 2) Stable, fast convergent numerical schemes were used in solving the complicated mathematical model. A combined utilization of finite difference and characteristic methods has been found to be a very useful method in handling hyperbolic partial differential equations and their extraneous boundary conditions. 3) The pressure transients predicted by numerical calculation are in close agreement with the $P(t,x)$ results obtained experimentally. The theoretical prediction of the rupture time of the diaphragm, which seals the chamber at the end opposite the igniter, is also in very good agreement with the actual measured rupture times from separate firings. This indicates agreement between the predicted and measured speed of propagation of the convective burning wave. Moreover, the predicted percentage of propellant consumed during the flame spreading interval also compares favorably with the actual measured values. 4) The main features of the combustion waves are: a) driven by the internal pressure gradient, the flame advances by convection into pores; b) in the physical model considered, flame speed is never constant, the wave accelerates continuously; c) the pressure distribution displays a continental divide, where gas flows in opposite directions from peak; d) the flame zone is very thick and is determined by the gas permeability and particle size. 5) Burning velocities on the order of 1000 times the normal propellant burning velocities can be controlled and applied to rocket propulsion. The calculated speed of the transient flame front near the diaphragm location is 0.15 mm/μsec, which is still lower than that of LVD (on the order of 1 to 2 mm/μsec). However, if a longer chamber length, together with a stronger diaphragm, is used, the speed of the flame front may quickly reach the value in the transition to LVD region. Hence, this investigation may also pertain to the initiation of LVD and DDT.

Appendix

The numerical values used in the theoretical calculations are as follows

$r_t = 0.476$ cm		$\rho_p = 1.6$ g/cm^3	$\phi_o = 0.377$
$x_p = 0.579$ cm		$x_e = 3.81$ cm	$\gamma = 1.26$
$r_{p_o} = 0.267$ mm		$T_f = 2860$°K	$T_{\text{ign}} = 2645$°K
$T_o = 294$°K		$P_o = 1$ atm	$Pr = 0.7$
$R = 0.02926$ cal/g-°K		$k_p = 5.3 \times 10^{-4}$ cal/cm-sec-°K	
$\mu = 0.223 \times 10^{-3}$ g/cm-sec		$c_c = 0.35$ cal/g-°K	
$T_{\text{ablation}} = 450$°K		$T_{\text{ignition}} = 615$°K	
$c_d(r_{p_o}) = 12.5\%$		$\theta = 0.6$	

The thickness of deterred layer is equal to 0.0534 mm. The burning rate law for 30% deterred propellant is $r_b = 1.871P^{0.802}$ and for undeterred propellant is $r_b = 12.1P^{0.8867}$ where P is in kbar and r_b in cm/sec.

The chemical composition of the ball propellant used in the experiments is tabulated in Table 1.

Table 1

Ball propellant ingredients	%
Nitroglycerin	9.71
Dinitrotoluene	0.71
Diphenylamine	0.90
Dibutylphalate	5.96
Nitrocellulose (13.15% N)	81.05
Moisture and volatiles	0.85
Residual solvent	0.29
Calcium carbonate	0.46
Sodium sulfate	0.07

References

[1] Griffiths, B. N. and Groocock, J. M., "The Burning to Detonation of Solid Explosives," *Journal of the Chemical Society*, Vol. 814, 1960, p. 4154.

[2] Obmenin, A. V., Korotkov, A. I., Sulimov, A. A., and Dubovitskii, V. F., "Nature of Spreading in Predetonation Regimes of Porous Explosives," *Journal of Combustion, Explosion and Shock Waves*, Vol. 5, No. 4, Dec. 1969, pp. 461–470.

[3] Squire, W. H. and Devine, M. P., "The Interface Between Primer and Propellant," AOA Paper, 1969, published by Frankford Arsenal, Philadelphia, Pa.

[4] Andreev, K. K., *Experimental Investigation of the Combustion of Explosives*, the Academy of Sciences USSR, Moscow, Vol. 29, 1940, p. 469.

[5] Andreev, K. K., "The Problem of the Mechanism of Transition from Burning to Detonation in Explosives," *Journal of Physical Chemistry*, Vol. 17, Sept. 1944, pp. 533–537.

[6] Andreev, K. K., "Experimental Investigation of Burning of Secondary Explosives," *Collection of Papers on the Theory of Explosives*, Oborongiz, 1940, p. 39.

[7] Andreev, K. K., "On Dependence of Burning Rate of Secondary and Ignition Explosives on Pressure," *Doklady Akademii Nauk*, Vol. 51, No. 1, 1946, p. 29.

[8] Belyaev, A. F., "Mechanism of the Burning of Explosives," Doctor's Dissertation, 1946, Inst. of Chemical Physics, Academy of Sciences, U.S.S.R.

[9] Taylor, J. W., "The Burning of Secondary Explosive Powders by a Convective Mechanism," *The Faraday Society*, Vol. 58, No. 471, March 1962, pp. 561–568.

[10] Margolin, A. D., "Stability of Burning of Porous Explosives," *Doklady Akademii Nauk SSSR*, Vol. 140, No. 4, 1961, pp. 867–869.

[11] Godai, T., "Flame Propagation Into the Crack of Solid Propellant Grain," *AIAA Journal*, Vol. 8, No. 7, July 1970, pp. 1322–1327.

[12] Margolin, A. D. and Chuiko, S. V., "Combustion Instability of a Porous Charge with Spontaneous Penetration of the Combustion Products into the Pores," *Journal of Combustion, Explosion and Shock Waves*, Vol. 2, No. 3, 1966, pp. 119–124.

[13] Gipson, R. W. and Macek, A., "Flame Fronts and Compression Waves During Transition from Deflagration to Detonation in Solids," *Eighth Symposium (International) on Combustion*, The Combustion Inst., 1959, pp. 847–854.

[14] Hubbard, H. W. and Johnson, M. H., "Ignition of Detonations," *Journal of Applied Physics*, Vol. 30, 1959, pp. 765–769.

[15] Enig, J. W. and Metcalf, F. T., "Theoretical Calculations on the Shock Initiation of Solid Explosives," NOLTR-62-160, 1962, Naval Ordnance Lab., White Oak, Silver Spring, Md.

[16] Zel'dovich, Ya. B., "On the Theory of Combustion of Powder and Explosives," *Journal of Experimental and Theoretical Physics*, Vol. 12, No. 11–12, 1942.

[17] Belyaev, A. F., Korotkov, A. I. and Sulimov, A. A., "Breakdown of Surface Burning of Gas-Permeable Porous Systems," *Journal of Combustion, Explosion and Shock Waves*, Vol. 2, No. 3, 1966, p. 21.

[18] Belyaev, A. F., "Combustion, Detonation and the Work of Condensed Explosive Systems," Science Publisher, Moscow, 1968, Chap. 8.

[19] Obmenin, A. V., Korotkov, A. I., Sulimov, A. A. and Dubovitskii, V. F., "Nature of Spreading in Predetonation Regimes of Porous Explosives," *Journal of Combustion, Explosion and Shock Waves*, Vol. 5, No. 4, 1969.

[20] Bird, R. B., Stewart, W. E., and Lightfoot, E. N., "Interphase Transport in Isothermal System," *Transport Phenomena*, 7th ed., Wiley, New York, 1966, pp. 196–200.

[21] Eckert, E. R. G. and Drake, Jr., R. M., *Heat and Mass Transfer*, McGraw-Hill, New York, 1959, pp. 248–253.

[22] Vichnevetsky, R., "Treatment of Boundary Conditions in Difference Methods for One-Dimensional Fluid Dynamics Equations," TR 70-21, Sept. 1970, Electronics Associates Inc., West Long Branch, N.J.

[23] Vichnevetsky, R., "Treatment of the Chamber/Duct Boundary Conditions when the Gas Velocity Changes Sign," TR 71-7, Feb. 1971, Electronic Associates Inc., West Long Branch, N.J.

[24] Isaacson, E. and Keller, H. B., "Numerical Solution of Linear Systems and Matrix Inversion," *Analysis of Numerical Methods*, Wiley, New York, 1966, pp. 58–61.

[25] Vichnevetsky, R., and Tomalesky, A. W., "Spurious Wave Phenomena in Numerical Approximations of Hyperbolic Equations," *Proceedings of the Fifth Annual Princeton Conference on Information Science and Systems*, Princeton Univ., March 1971, pp. 1–7.

[26] Squire, W. H., private communication, 1970–1971, Frankford Arsenal, Philadelphia, Pa.